

Oscillations and confluence in three-magnon scattering of ferromagnetic resonance

Tao Qu,¹ Alex Hamill,^{2,*} R. H. Victora,¹ and P. A. Crowell²

¹*Department of Electrical and Computer Engineering,
University of Minnesota, Minneapolis, MN, 55455, USA*

²*School of Physics and Astronomy,
University of Minnesota, Minneapolis, MN, 55455, USA*

arXiv:2204.11969v4 [cond-mat.mes-hall] 31 Dec 2022

Abstract

We have performed a time-resolved and phase-sensitive investigation of three-magnon scattering of ferromagnetic resonance (FMR) over several orders of magnitude in excitation power. We observe a regime that hosts transient oscillations of the FMR magnon population, despite higher-order magnon interactions at large powers. Also at high powers, the scattering generates 180° phase shifts of the FMR magnons. These phase shifts correspond to reversals in the three-magnon scattering direction, between splitting and confluence. These scattering reversals are most directly observed after removing the microwave excitation, generating coherent oscillations of the FMR magnon population much larger than its steady-state value during the excitation. Our model is in strong agreement with these findings. These findings reveal the transient behavior of this three-magnon scattering process, and the nontrivial interplay between three-magnon scattering and the magnons' phases.

Magnons are the quanta of collective spin excitations. Their phase degree of freedom, highly nonlinear behavior [1–17], and long lifetimes make them an active subject in fundamental research [18–21] and research towards next-generation microwave and information technology [22–29]. A magnon mode's population (hereafter referred to as its amplitude) can be excited above a threshold value such that it becomes unstable, returning to the threshold value through three-magnon splitting [30]. This nonlinear process is referred to as the first-order Suhl instability.

The zero-wavevector magnon mode corresponds to ferromagnetic resonance (FMR) and has a dramatically low threshold amplitude for this instability, particularly in magnetic insulators due to their low damping. This allows for efficient excitation of finite-wavevector magnons and the study of nonlinear magnon interactions over a wide power range. However, little is known about how this instability evolves in time and the role of the excitation power. Previous experiments have observed no associated power-dependence [31], or have instead focused on the influence of dipole radiation [32] or of group velocity and proximity to the excitation antenna [33]. The reverse process of splitting is referred to as confluence, which also requires further investigation [33]. Its relationship with splitting is an unresolved question, as is the relationship between three-magnon scattering processes and the magnons' phases.

* hamil483@umn.edu

To this end, we employ time-resolved homodyning spectroscopy to examine this instability with phase-sensitivity over five orders of magnitude in microwave excitation power. We observe a regime hosting power-dependent transient oscillations of the FMR amplitude, that at high powers the instability induces 180° phase shifts of FMR, and that these phase shifts correspond to reversals between three-magnon splitting and confluence. Furthermore, turning off the microwave excitation stimulates such reversals, generating prolonged and coherent oscillations of the FMR amplitude. Our model is in strong agreement with these observations, and explains the origin of the oscillatory regime as well as the oscillations after turn-off. The oscillatory regime persists up to the highest powers employed, being remarkably robust against the higher-order interactions that arise.

The FMR mode b_0 with a frequency f_0 is subject to the first-order Suhl instability when magnon modes $b_{\pm\mathbf{k}_i}$ at $f_0/2$ are available. This occurs at low FMR frequencies for in-plane magnetized films, due to a minimum in the magnon dispersion [34, 35]; an increase in wavenumber suppresses the dynamic demagnetization field. With these modes available, b_0 becomes unstable above a threshold amplitude and undergoes three-magnon splitting to $b_{\pm\mathbf{k}_i}$. In the reverse process, confluence, two magnons $b_{\pm\mathbf{k}_i}$ combine into a magnon b_0 [Fig. 1(a)].

We investigated this instability in the time domain through homodyning spectroscopy [Fig. 1(b)]. The microwave excitation at the desired FMR frequency f_0 is converted to the desired applied microwave power P_a and to $8\ \mu\text{s}$ pulses using an attenuator and switch. These pulses enter a wide microstrip waveguide, generating a spatially uniform microwave magnetic field of amplitude h_a throughout the sample: a $3\ \mu\text{m}$ -thick film of Yttrium Iron Garnet (YIG). We resonantly excite the sample's FMR mode by matching its FMR frequency with f_0 , via tuning the static magnetic field H to H_0 . We primarily investigated the transient behavior at $f_0 = 1.5\ \text{GHz}$, with a corresponding resonant field of $H_0 = 135.1\ \text{Oe}$. The sample is inductively coupled to the microstrip, such that its FMR response b_0 induces a corresponding voltage in the microstrip [36]. We obtain the envelope of the microstrip's output voltage by mixing it with a phase- and frequency-matched reference. By subtracting the output voltage's envelope at resonance from that at zero field, we isolate the envelope of the voltage induced by FMR. When nonlinearity-induced phase shifts are absent, this envelope directly corresponds to the FMR amplitude $c_0(t)$ with the susceptibility $\chi''(t) = c_0(t)/h_a \propto c_0(t)/\sqrt{P_a}$. For additional experimental details, see Sec. 1 of the supplementary

material (SM).

To verify our experiment, we compare the measured steady-state susceptibility χ''_{∞} with Suhl's theory [30] around the instability's threshold power P_S [see Fig. 1(c)]. For $P_a < P_S$, c_0 is in the linear regime, such that its steady-state value is proportional to h_a . For $P_a = P_S$, this value corresponds to c_S , the threshold amplitude for the (nonlinear) instability regime. The steady-state value of c_0 saturates at c_S in the nonlinear regime, as three-magnon splitting occurs for $c_0 > c_S$. As such, as P_a is increased, χ''_{∞} decreases as $\chi''_{\infty} \propto 1/\sqrt{P_a}$. We compare this with the experimental results by normalizing χ''_{∞} to its value in the linear regime χ''_L . The experimentally obtained saturation from both steady-state (using lock-in techniques) and time-resolved measurements is in reasonable agreement with the theoretical prediction.

In our time-resolved measurements [Fig. 1(d)], we find both the linear and nonlinear regimes as well as their expected transient behavior: in the linear regime (purple curve) c_0 rises monotonically to its steady-state value, while in the nonlinear regime (blue curve) it becomes unstable and then relaxes to c_S via three-magnon splitting. However, we observe

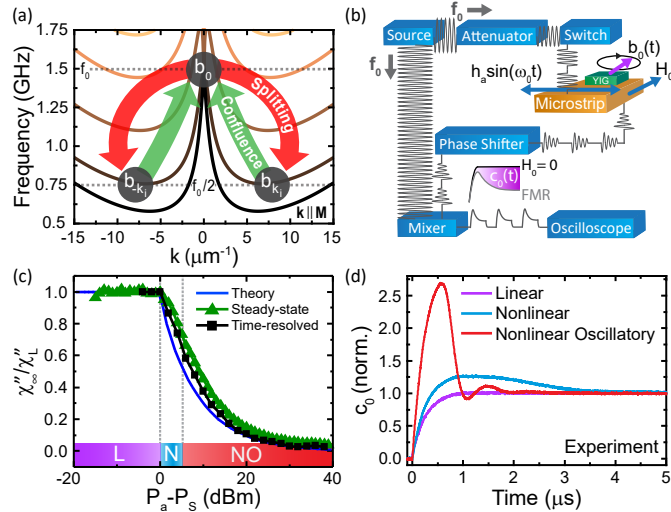


FIG. 1. (a) The magnon dispersion of $3 \mu\text{m}$ YIG films magnetized in-plane, in 15° increments of the angle between the wavevector \mathbf{k} and the static magnetization \mathbf{M} . (b) Schematic diagram of the experiment. (c) $\chi''_{\infty}(P_a)/\chi''_L$ predicted from Suhl's theory (blue) and that measured through lock-in techniques (green) and time-resolved measurements (black). The color-coded regions correspond to the Linear (L), Nonlinear (N), and Nonlinear Oscillatory (NO) regimes. (d) Overview of the transient behavior of the FMR magnon population c_0 in each regime, normalized to the values of c_0 at steady state.

an additional regime with a threshold power $P_{osc} > P_S$, in which c_0 oscillates at a power-dependent frequency as it relaxes to c_S (red curve).

To understand this regime, we have developed a model for three-magnon scattering of FMR in thin films, for the case of resonant excitation by a perpendicular microwave field (see Sec. 2 of SM for details). We derive the associated equation of motion for the circularly-polarized magnetization m^+ via the Landau-Lifshitz equation. We then perform a plane-wave expansion of m^+ [30] to obtain the equations of motion of the circularly-precessing magnon modes. Afterwards, we employ a classical Bogoliubov transformation [37] to obtain the equations of motion of the eigenmodes, the elliptically-precessing magnon modes $b(\mathbf{k})$. We only retain terms up to second-order in the magnon modes, to account for three-magnon scattering while neglecting higher-order interactions. We account for linear damping of $b(\mathbf{k})$ through the relaxation rate $\eta(\mathbf{k}) = \omega(\mathbf{k})\epsilon(\mathbf{k})\alpha$ [38]; $\omega(\mathbf{k})$ is the mode's angular frequency, $\epsilon(\mathbf{k}) = \frac{1}{\gamma} (\partial\omega/\partial H)|_{\mathbf{k}, H_0}$ is the ellipticity factor, γ is the gyromagnetic ratio, and α is the measured Gilbert damping constant. We only consider the resulting equations of motion of the FMR mode b_0 and the N_k magnon modes $b_{\mathbf{k}_i}$ of frequency $f_0/2$ in the magnon dispersion. Each of these half-frequency modes' equation of motion is distinguished by $\zeta_{\mathbf{k}_i}$, their coupling strength with b_0 , and their relaxation rate $\eta_{\mathbf{k}_i}$. However, these distinguishing parameters have weak variation among the $f_0/2$ modes. Hence, we set $\zeta_{\mathbf{k}_i}$ and $\eta_{\mathbf{k}_i}$ to their average value over all $f_0/2$ modes, $\bar{\zeta}, \bar{\eta}_k$. This causes the equations of motion for each of the half-frequency modes to be identical, reducing the N_k half-frequency modes to a single effective mode b_k . Note that we also equate $b_k(t)$ and $b_{-k}(t)$, as the splitting and confluence processes affect each mode equally. This reduces our model to the two equations of motion

$$\dot{b}_0 = (i\omega_0 - \eta_0)b_0 - N_k \bar{\zeta} b_k^2 + \nu h_a e^{i(\omega_0 t - \pi/2)}, \quad (1)$$

$$\dot{b}_k = (i\omega_k - \bar{\eta}_k)b_k + \bar{\zeta} b_k^* b_0. \quad (2)$$

ν is the coupling of b_0 to the microwave field. The magnon mode's response b_i ($i = 0, k$) encodes both its amplitude $|b_i|$ and its phase, such that $b_i(t) = |b_i(t)|e^{i(\omega_i t + \theta_i + \phi_i(t))}$. $\theta_{0,k} = -\pi/2, -\pi/4$ are the modes' phase offsets for the cases of linearity and weak nonlinearity, as found from numerically solving Eqs. (1),(2). $\phi_i(t)$, discussed later, will correspond to phase shifts induced by strong nonlinearity. We define $c_i(t)$ as the mode's amplitude for $\phi_{0,k} = 0$, such that $b_i(t) = c_i(t)e^{i(\omega_i t + \theta_i)}$. Inserting this relation into Eqs. (1),(2) yields the equations

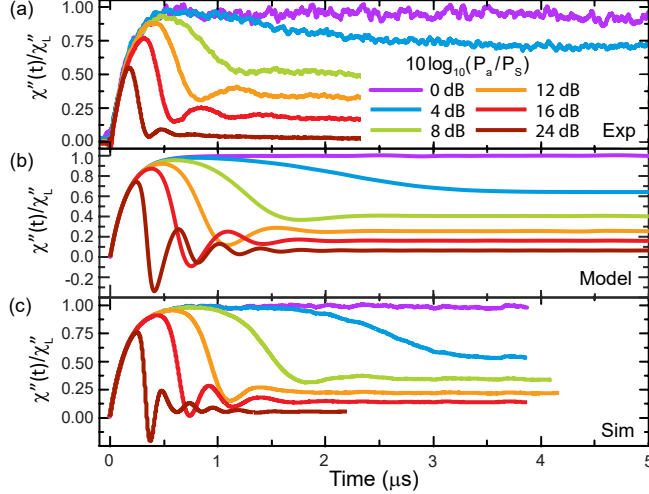


FIG. 2. Comparison of the FMR amplitude's transient behavior from (a) the experiment, (b) the numerical solutions to Eqs. (3),(4), and (c) the micromagnetic simulations. The FMR amplitude c_0 is normalized to $\chi''(t)/\chi_L''$ to enable direct comparison between each approach.

of motion for the magnon mode amplitudes:

$$\dot{c}_0 = -\eta_0 c_0 - N_k \bar{\zeta} c_k^2 + \nu h_a, \quad (3)$$

$$\dot{c}_k = -\bar{\eta}_k c_k + \bar{\zeta} c_k c_0. \quad (4)$$

This definition of c_0 , as in the experiment, corresponds to the envelope of b_0 obtained by mixing it with a frequency-matched reference signal $e^{-i(\omega_0 t + \theta_0)}$. As such, the experiment can be directly compared with the numerical solutions of Eq. (3). For numerically solving our equations of motion, we set the value of h_a such that h_a/h_S matches the experiment and simulations; h_S is the observed threshold value of h_a for the instability. η_i is calculated as described previously. All other parameters are set to the values calculated from our model. See Sec. 2 of SM for their derivations. The initial values are the thermal amplitudes corresponding to the Bose-Einstein distribution (see Sec. 3 of SM). For details on the simulations and numerical solutions, see Sec. 4 of SM.

Figure 2 compares the time-evolution of c_0 from the experiment, the numerical solutions of Eqs. (3),(4), and the micromagnetic simulations. We normalize to $\chi''(t)/\chi_L''$ for direct comparison between each approach. Each curve color corresponds to the same relative power P_a/P_S . The purple and blue curves correspond to the linear and nonlinear regimes, while the green curves correspond to the entrance into the nonlinear oscillatory regime. As P_a is increased, the oscillation frequency f_{osc} monotonically increases while the timescale of

the initial transient peak monotonically decreases. Strong qualitative agreement is observed between each approach, which is also the case at 2.5 GHz (see Sec. 5 of SM). The oscillations weaken as one goes from the model to simulation to experiment, presumably due to increasing magnon dephasing. In addition to simulations allowing for other magnon interactions, they include thermal fluctuations which can lead to dephasing. In the experiment, additional dephasing may arise from sample and magnetic field inhomogeneity.

To analyze the oscillatory regime, we linearize Eqs. (3),(4) by Taylor expanding \dot{c}_0, \dot{c}_k about the nonlinear regime's fixed point, which corresponds to steady state; this allows us to treat the second-order terms as negligible. We then impose a time-dependence of the form $c_0, c_k \propto e^{\lambda t}$, and solve for λ . The transition to the oscillatory regime corresponds to the nonlinear regime's fixed point changing from a stable node to a stable spiral, such that λ becomes complex. This transition can be thought of as the point where the splitting rate becomes large enough to produce negative feedback by suppressing c_0 to below c_S , where splitting is suppressed. This generates exchanges in dominance between the splitting and the microwave excitation terms in Eq. (3), hence the oscillations. This analysis (see Sec. 6 of SM) yields predicted values for the oscillation frequency f_{osc} and the threshold value of h_a for the oscillatory regime, h_{osc} :

$$f_{osc} = \eta_0 \sqrt{\frac{\bar{\zeta}\nu}{8\pi^2}(h_a - h_{osc})}, \quad (5)$$

$$h_{osc} = h_S \left(1 + \frac{\eta_0}{8\bar{\eta}_k}\right). \quad (6)$$

We compare the predicted scaling from Eq. (5) with our results by extracting, via a Fourier transform, the oscillations' frequency spectra from each approach [Figs. 3(a,b)]. We define f_{osc} at each power as the characteristic peak in the oscillations' frequency spectra and h_{osc} as the value of h_a just below where low-frequency structure is observed in the spectra. For more details, see Sec. 7 of SM. The linearized model's predicted scaling $f_{osc} \propto \tilde{h}^{0.5}$, where $\tilde{h} = (h_a - h_{osc})/h_{osc}$, is compared to the scaling obtained from each approach [Fig. 3(c)]. We normalize $h_a - h_{osc}$ by h_{osc} to directly compare each approach. The model's results are from the numerical solutions of Eqs. (3), (4). The filled symbols are those included in the scaling fit (dashed lines) such that quantitative agreement with Eq. (5) is observed. The range of agreement for each approach is several orders of magnitude in P_a . This is also the case for $f_0 = 2.5$ GHz (see Sec. 5 of SM). The oscillation frequencies in the experiment and simulations show good agreement, but they are larger than those from our model. This is

likely due to an incomplete treatment of damping and/or an underestimation of $\bar{\zeta}$, as we neglect the full Gilbert damping term and spatial variation of the longitudinal magnetization component.

As the relative power $10 \log_{10}(P_a/P_{osc})$ increases to 14 dB, the oscillations' frequency spectra broaden in the experiment and simulations [Figs. 3(a,b)]. To investigate this, we compare the simulations' magnon mode amplitudes $c(\mathbf{k})$ [39] at the relative powers of 2 dB (no broadening) and 25 dB (pronounced broadening) [Fig. 3(d)]. At 2 dB, only the $f_0/2$ modes with the largest coupling strengths $\zeta_{\mathbf{k}_i}$ are excited. Note that the coupling is strongest for the modes with wavevectors most misaligned with the static magnetization \mathbf{M} . At 25 dB, the weaker-coupled $f_0/2$ modes are also excited, with some even exceeding the amplitude of the strongest-coupled modes. The excited modes also exhibit a wider frequency distribution about $f_0/2$, which may generate the observed broadening. The most straightforward explanation for this transition is the onset of four-magnon scattering of $f_0/2$, opposite-wavevector pairs of magnons at the strongest-coupled modes to such pairs at

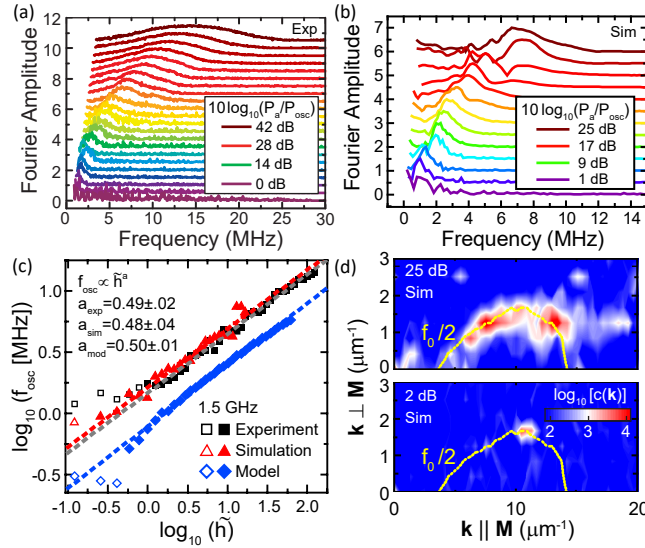


FIG. 3. Oscillation analysis at $f_0 = 1.5$ GHz. (a,b) Normalized and offset frequency spectra of the oscillations in (a) the experiment, and (b) the simulations, with a 2 dB increment between curves. (c) The scaling of the oscillation frequency f_{osc} for each approach. The filled symbols indicate the fitted region and have a spacing of 1 dB in power. (d) The simulations' magnon mode amplitudes $c(\mathbf{k})$ for powers 2 dB (bottom, no broadening) and 25 dB (top, with broadening) greater than P_{osc} .

weaker-coupled modes, which conserves energy and momentum.

At the highest powers, the splitting becomes pronounced enough to introduce negative values of c_0 [Figs. 4(a,b)]. As c_0 is phase-sensitive, being obtained by mixing b_0 with a reference signal, this corresponds to b_0 undergoing a phase shift $\phi_0 \sim 180^\circ$. Phase shifts for the mode b_i arise when its response is dominated by its scattering term [see Eqs. (1),(2)], such that it is strongly nonlinear. At these powers, we also observe pronounced oscillations of c_0 after turning off the microwave excitation. Notably, these oscillations' amplitudes greatly exceed the steady-state value of c_0 during excitation and they persist for roughly 600 ns. Each curve in Figs. 4(a,b) is normalized to the turn-on peak at the highest power, showing the oscillations at excitation turn-on and turn-off to be comparable in size. To understand these observations, we examine the case of strong nonlinearity in our model by numerically solving Eqs. (1),(2), which provides the evolution of the modes' amplitudes as well as their phases. We calculate the modes' phase shifts $\phi_i(t)$ by using our general definition $b_i(t) = |b_i(t)|e^{i(\omega_i t + \theta_i + \phi_i(t))}$:

$$\phi_i(t) = \frac{1}{i} \ln \left(\frac{b_i(t)}{|b_i(t)|} e^{-i(\omega_i t + \theta_i)} \right). \quad (7)$$

The evolution of the amplitudes and phase shifts is shown in Figs. 4(c,d) and Figs. 4(e,f); we utilize $|\phi_i(t)|$ for simplicity. For consistency with the experiment, we plot c_0 instead of $|b_0|$, taking $c_0(t) = \text{Re}(b_0(t)e^{-i(\omega_0 t + \theta_0)})$.

After turning on the excitation [Figs. 4(c,e)], we find π phase shifts of ϕ_0 at $c_0 = 0$, with these phase shifts triggering variation in ϕ_k . We first examine the influence of the π phase shift on the amplitudes' equations of motion. Whereas $c_i(t)$ is the mode's amplitude for $\phi_{0,k} = 0, 0$, we define $c'_i(t)$ as the mode's amplitude for $\phi'_{0,k} = \pi, 0$. Substituting $b_i(t) = c'_i(t)e^{i(\omega_i t + \theta_i + \phi'_i)}$ into Eqs. (1),(2) yields the amplitudes' new equations of motion given the π phase shift:

$$\dot{c}'_0 = -\eta_0 c'_0 + N_k \bar{\zeta} c_k'^2 - \nu h_a, \quad (8)$$

$$\dot{c}'_k = -\bar{\eta}_k c'_k - \bar{\zeta} c'_k c'_0. \quad (9)$$

Comparison with Eqs. (3),(4) shows that the π phase shift switches the sign of both the microwave field term νh_a and the three-magnon scattering terms $\sim \bar{\zeta}$. From the latter, it is evident that these phase shifts correspond to reversals in the three-magnon scattering direction between splitting and confluence. The reversals to confluence explain why $|c_0(t)|$

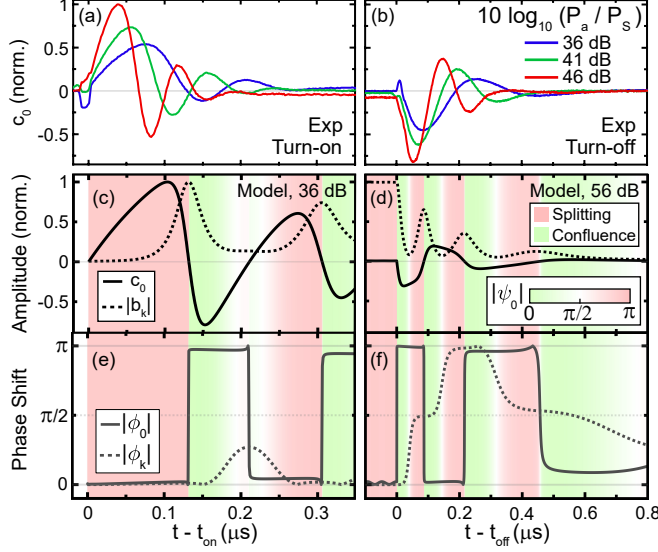


FIG. 4. (a,b) The experimental results for $c_0(t)$ at high powers when turning on and off the microwave excitation. Each curve is normalized to the peak amplitude at turn-on for the relative power of 46 dB. (c,d) The magnon amplitudes c_0 , $|b_k|$, with each time color-coded for the corresponding value of $|\psi_0|$. Note that c_0 at turn-off is instead normalized to the peak amplitude at turn-on for the relative power of 56 dB. (e,f) The corresponding phase shifts $|\phi_{0,k}|$.

increases with time despite being damped by the now out-of-phase microwave field for $c_0 < 0$ [Figs. 4(a,c)]. Furthermore, they explain the variation of ϕ_k : with $|b_k(t)|$ being suppressed by confluence, its three-magnon scattering dominates over its linear terms such that b_k enters the strong nonlinearity regime.

These reversals are more directly evident after turning off the microwave excitation, where $|c_0(t)|$ undergoes a pronounced increase in time despite the absence of the excitation field. Furthermore, without the microwave field to drive ϕ_0 back to 0° , the variations of ϕ_k evolve into 90° phase shifts of b_k , generating additional reversals [Figs. 4(d,f)]. The $180^\circ, 90^\circ$ phase shifts of b_0, b_k are those required to reverse the scattering direction, with the factor-of-two difference being due to the same factor difference in their frequencies. These reversals explain both the pronounced oscillations of c_0 at turn-off and the oscillations' enhancement with microwave power: the scattering at turn-off, and hence the reversals, are driven by the steady-state values of c_0, c_k during turn-on, where $c_k \propto \sqrt{h_a - h_S}$ at steady state [see Eq. (61) in SM]. The model's turn-off oscillations of c_0 are much weaker than those in the experiment, hence the use of the higher relative power of 56 dB. This may be because of our

use of a linear damping term $-\eta_i b_i$, which is insensitive to phase shifts, instead of the full Gilbert damping term.

To determine how the scattering direction evolves in time, we consider the relative phase $|\psi_i(t)|$ between b_i and the three-magnon scattering term in its equation of motion. As with the linear damping term $-\eta_i b_i$, the damping of b_i by scattering corresponds to the scattering term being π out-of-phase with b_i . Conversely, the scattering term drives b_i when it is in-phase with b_i . As such, $|\psi_0| = 0, \pi$ corresponds to confluence and splitting, respectively, and we can calculate $|\psi_0(t)|$ to determine the evolution of the scattering direction. Note that $|\psi_0(t)|$ and $|\psi_k(t)|$ are found to mirror each other about $\pi/2$ as expected, such that one mode is being driven by scattering while the other mode is being damped. From Eq. (1), $\psi_0(t)$ takes the form

$$\psi_0(t) = \frac{1}{i} \ln \left(\frac{b_0(t)/|b_0(t)|}{b_k^2(t)/|b_k^2(t)|} \right). \quad (10)$$

$|\psi_0(t)|$ corresponds to the color-coding in Figs. 4(c-f). The switching of $|\psi_0(t)|$ between $0, \pi$ aligns with the phase shifts and the transitions between growth and decay of $b_k(t)$ as expected, verifying that the relative phase $|\psi_i(t)|$ indicates the three-magnon scattering direction.

In summary, for three-magnon scattering of ferromagnetic resonance, we observe a regime that hosts transient oscillations of the magnon populations, with the transient behavior being highly dependent on the excitation power. At high excitation powers, we find that the scattering generates significant phase shifts of the magnons and that these phase shifts correspond to reversals between three-magnon splitting and confluence. Such reversals also occur upon turning off the excitation, generating prolonged and coherent oscillations. Our model captures these behaviors. These findings shed light on the transient behavior of this instability, and reveal the nontrivial interplay between three-magnon scattering and the magnons' phases.

The authors thank Aneesh Venugopal for fruitful discussion on efficient computation in the micromagnetic simulations and Cody Schimming for valuable mathematical insight. The Minnesota Supercomputing Institute (MSI) provided resources that contributed to the research results reported within this article. The authors acknowledge support by SMART, a center funded by nCORE, a SRC program sponsored by NIST. The authors also acknowledge support by DARPA under Grant W911NF-17-1-0100, MINT at Minnesota, and the NSF

XSEDE through Allocation No. TG-ECS200001.

T. Q. and A. H. contributed equally to this work.

-
- [1] S.M. Rezende and F.M. de Aguiar, Spin-wave instabilities, auto-oscillations, and chaos in yttrium-iron-garnet, *Proc. IEEE* **78**, 893 (1990).
 - [2] P. Wigen, R. McMichael, and C. Jayaprakash, Route to chaos in the magnetic garnets, *J. Magn. Magn.* **84**, 237 (1990).
 - [3] I. Laulicht and P. Wigen, On the transient and stationary parametric excitation of spin waves, *J. Magn. Magn.* **207**, 103 (1999).
 - [4] C. Mathieu, V.T. Synogatch, and C.E. Patton, Brillouin light scattering analysis of three-magnon splitting processes in yttrium iron garnet films, *Phys. Rev. B* **67**, 104402 (2003).
 - [5] S.Y. An, P. Krivosik, M.A. Kraemer, H.M. Olson, A.V. Nazarov, and C.E. Patton, High power ferromagnetic resonance and spin wave instability processes in Permalloy thin films, *J. Appl. Phys.* **96**, 1572 (2004).
 - [6] P. Kabos, G. Wiese, and C. Patton, Measurement of spin wave instability magnon distributions for subsidiary absorption in yttrium iron garnet films by Brillouin light scattering, *Phys. Rev. Lett.* **72**, 2093 (1994).
 - [7] A. Krawiecki and A. Sukiennicki, On-off intermittency and peculiar properties of attractors in a simple model of chaos in ferromagnetic resonance, *Acta Phys. Pol. A* **2**, 269 (1995).
 - [8] T.L Carroll, L.M Pecora, and F.J Rachford, Chaos in magnetostatic modes in an yttrium iron garnet film between 2 and 4 GHz, *J. Appl. Phys.* **67**, 5630 (1990).
 - [9] T.L Carroll, L.M Pecora, and F.J Rachford, Chaos and chaotic transients in an yttrium iron garnet sphere, *Phys. Rev. A* **40**, 377 (1989).
 - [10] T.L Carroll, L.M Pecora, and F.J Rachford, Chaotic transients and multiple attractors in spin-wave experiments, *Phys. Rev. Lett.* **59**, 2891 (1987).
 - [11] W. Araujo, F. de Aguiar, A. Azevedo, and S. Rezende, Dual pumping of magnetostatic and spin-wave modes in yttrium-iron-garnet spheres, *J. Appl. Phys.* **93**, 8752 (2003).
 - [12] G. Srinivasan, M. Chen, and C. Patton, Observation of auto-oscillations and chaos in subsidiary absorption in yttrium iron garnet, *J. Appl. Phys.* **64**, 5480 (1988).

- [13] V.E. Zakharov, V. L'vov, and S. Starobinets, Spin-wave turbulence beyond the parametric excitation threshold, *Sov. Phys. Uspekhi* **17**, 896 (1975).
- [14] V.B Cherepanov and A.N Slavin, Collective spin-wave oscillations in finite-size ferromagnetic samples, *Phys. Rev. B* **47**, 5874 (1993).
- [15] S. Rezende, F. de Aguiar, and A. Azevedo, Spin-wave auto-oscillations still in need of a good model, *J. Appl. Phys.* **67**, 5624 (1990).
- [16] A.N Slavin, G. Srinivasan, S. Cordone, and V.B Cherepanov, Instability mechanism of collective spin wave oscillations in finite-size ferrite samples, *J. Appl. Phys.* **75**, 5610 (1994).
- [17] V.T. Synogach, Y.K. Fetisov, C. Mathieu, and C.E. Patton, Ultrashort microwave pulses generated due to three magnon interactions, *Phys. Rev. Lett.* **85**, 2184 (2000).
- [18] Roman V. Verba, Lukas Körber, Katrin Schultheiss, Helmut Schultheiss, Vasil Tiberkevich, and Andrei N. Slavin, Theory of three-magnon interaction in a vortex-state magnetic nanodot, *Phys. Rev. B* **103**, 014413 (2021).
- [19] Barsukov, I., Lee, H.K., Jara, A.A., Chen, Y-J., Gonçalves, A.M., Sha, C., Katine, J.A., Arias, R.E., Ivanov, B.A., and Krivorotov, I.N., Giant nonlinear damping in nanoscale ferromagnets, *Sci. Advc.* **5**, eaav6943 (2019).
- [20] Schultheiss, K., Verba, R., Wehrmann, F., Wagner, K., Körber, L., Hula, T., Hache, T., Kákay, A., Awad, A.A., Tiberkevich, V., and others, Excitation of whispering gallery magnons in a magnetic vortex, *Phys. Rev. Lett.* **122**, 097202 (2019).
- [21] T.X. Zhou, J.J. Carmiggelt, L.M. Gächter, I. Esterlis, D. Sels, R.J. Stöhr, C. Du, D. Fernandez, J.F. Rodriguez-Nieva, F. Büttner, *et al.*, A magnon scattering platform, *Proc. Nat. Acad. Sci. USA* **118** (2021).
- [22] Serga, A.A and Chumak, A.V and Hillebrands, B, YIG magnonics, *J. Phys. D* **43**, 264002 (2010).
- [23] J.D. Adam and S.N. Stitzer, Frequency selective limiters for high dynamic range microwave receivers, *IEEE Trans. Microw. Theory Tech.* **41**, 2227 (1993).
- [24] J.D. Adam and F. Winter, Magnetostatic wave frequency selective limiters, *IEEE Trans. Magn.* **49**, 956 (2013).
- [25] P. Pirro, V.I. Vasyuchka, A.A. Serga, and B. Hillebrands, Advances in Coherent Magnonics, *Nat. Rev. Mater.* **6**, 1114–1135 (2021).
- [26] A. Barman, G. Gubbiotti, S. Ladak, A.O. Adeyeye, M. Krawczyk, J. Gräfe, C. Adelman,

- S. Cotofana, A. Naeemi, V.I. Vasyuchka, *et al.*, The 2021 magnonics roadmap, *J. Phys. Condens. Matter* (2021).
- [27] G. Csaba, Á. Papp, and W. Porod, Perspectives of using spin waves for computing and signal processing, *Phys. Lett. A* **381**, 1471 (2017).
- [28] Chumak, Andrii V, Magnon spintronics: Fundamentals of magnon-based computing, in *Spintronics Handbook: Spin Transport and Magnetism, Second Edition* (CRC Press, 2019) pp. 247–302.
- [29] A. Etesamirad, R. Rodriguez, J. Bocanegra, R. Verba, J. Katine, I. Krivorotov, V. Tyberkevych, B. Ivanov, and I. Barsukov, Controlling Magnon Interaction by a Nanoscale Switch, *ACS Appl. Mater. Interfaces* **13**, 20288-20295 (2021).
- [30] H. Suhl, The theory of ferromagnetic resonance at high signal powers, *J. Phys. Chem. Solids* **1**, 209 (1957).
- [31] R. Cunha, J. Holanda, L. Vilela-Leão, A. Azevedo, R. Rodríguez-Suárez, and S. Rezende, Nonlinear dynamics of three-magnon process driven by ferromagnetic resonance in yttrium iron garnet, *Appl. Phys. Lett.* **106**, 192403 (2015).
- [32] B. Desormière, E. Milot, and H. Le Gall, Transient processes in spin-wave systems with magnetic dipole radiation-II. Experimental investigations*, *J. Phys. Chem. Solids* **30**, 1135-1146 (1969).
- [33] H.J. Liu, G.A. Riley, C.L. Ordóñez-Romero, B.A. Kalinikos, and K.S. Buchanan, Time-resolved study of nonlinear three-magnon processes in yttrium iron garnet films, *Phys. Rev. B* **99**, 024429 (2019).
- [34] B. Kalinikos and A.N Slavin, Theory of dipole-exchange spin wave spectrum for ferromagnetic films with mixed exchange boundary conditions, *J. Phys. C* **19**, 7013 (1986).
- [35] M. Mansuripur and R. Giles, Demagnetizing field computation for dynamic simulation of the magnetization reversal process, *IEEE Trans. Magn.* **24**, 2326 (1988).
- [36] I.S. Maksymov and M. Kostylev, Broadband stripline ferromagnetic resonance spectroscopy of ferromagnetic films, multilayers and nanostructures, *Physica E Low Dimens. Syst. Nanostruct.* **69**, 253 (2015).
- [37] A. Y. Dobin and R. H. Victora, Intrinsic nonlinear ferromagnetic relaxation in thin metallic films, *Phys. Rev. Lett.* **90**, 167203 (2003).
- [38] V. Kambersky and C. E. Patton, Spin-wave relaxation and phenomenological damping in

ferromagnetic resonance, *Phys. Rev. B* **11**, 2668 (1975).

- [39] T. Qu, A. Venugopal, J.M. Etheridge, W.K. Peria, K. Srinivasan, B.J. Stadler, P.A. Crowell, and R.H. Victora, Nonlinear magnon scattering mechanism for microwave pumping in magnetic films, *IEEE Access* **8**, 216960 (2020).

Supplementary Material: Oscillations and confluence in three-magnon scattering of ferromagnetic resonance

1. EXPERIMENTAL METHODS

The experiment was performed on a commercially obtained [1] 3 μm -thick YIG film grown by liquid phase epitaxy on a GGG substrate. A sample of 2 mm width and 5 mm length was obtained via a wafer saw, then centered (with the YIG side facing down) on top of a homemade microstrip waveguide of 3.4 mm strip width. We utilize a microstrip waveguide of larger width than the magnetic sample for microwave field homogeneity. This suppresses the excitation of millimeter-wavelength magnon modes, yielding an isolated FMR peak with no prominent satellite peaks and a linewidth $\Delta H \approx 0.3$ Oe. After characterizing the resonance through field-swept measurements, via a lock-in amplifier, time-resolved measurements at zero field and ferromagnetic resonance were performed with an oscilloscope. These measurements utilized homodyning spectroscopy as detailed below.

For our homodyning spectroscopy circuit, a microwave source provides a signal at the desired FMR frequency, which is then split into the RF and LO branches necessary for mixing. The LO branch goes directly to the LO port of the mixer to drive the mixer. Meanwhile, the signal in the RF branch is set to the desired power through the attenuator, and then converted via a switch from a steady signal to an 8 μs duration, 50% duty cycle pulsed signal. The pulsed RF signal is then fed into the microstrip waveguide, which is placed between the poles of an electromagnet. Due to inductive coupling to the waveguide, the magnetic response of the YIG can be measured as a voltage superimposed on the transmitted RF signal. The RF signal is then fed into a phase shifter such that the phases of the RF and LO branches are matched at their inputs to the mixer. Isolators are placed at the RF and LO inputs of the mixer to suppress reflections from the mixer. Due to the phase- and frequency-matching between the RF and LO ports, the output of the mixer corresponds to the envelope of the RF signal. This output is fed into a low-pass filter and terminated at the input of an oscilloscope or lock-in amplifier. To isolate the absorption voltage $V_{abs}(t)$, which corresponds to the FMR amplitude $c_0(t)$, the RF signals' envelopes at FMR are subtracted from those at zero field.

For the time-resolved measurements, the captured waveform is an average of 512 wave-

forms. The captured waveform contains several pulses, which are then averaged over as well. Lastly, small moving averages were applied to the data. The moving average window size went incrementally from 5 points at high powers to 50 points to low powers. Given the time resolution of 2-5 ns, these window sizes were selected so as to not impact the time behavior on timescales that are relevant to this study.

To directly compare the FMR amplitudes between different approaches, we normalize them to the absorptive susceptibility $\chi''(t) = c_0(t)/h_a$, which is normalized in turn to its steady-state value in the linear regime χ_L'' . In the experiment, $\chi''(t)$ was obtained by treating the absorption voltage $V_{abs}(t)$ and the applied microwave voltage amplitude V_a as proxies for c_0 and h_a . We also observe a voltage offset V_0 , which likely arises from leakage from the LO port to the RF port. This yields the relation $\chi_{exp}'' = V_{abs}/(V_a - V_0)$.

The experimental value of η_0 (defined here as $\eta_{0,exp}$) at each FMR frequency was found by fitting the linear behavior $c_0(t) \propto (1 - e^{-\eta_0 t})$ to the experimental data in the linear regime at multiple powers and averaging the fitted values of η_0 . Via the definition of η_i in the main text, the associated Gilbert damping constant is then calculated via the equation $\alpha_{exp} = \eta_{0,exp}/\omega_0\epsilon_0$. The simulations' timescales were then re-scaled by the value $\alpha_{sim}/\alpha_{exp}$, as an artificially large α_{sim} was used for computational efficiency. In addition, the measured value of $\eta_{0,exp}$ was the value of η_0 utilized in the numerical solving of our model. We also utilized the associated value of $\bar{\eta}_k$, which was calculated by treating the damping constant as independent of wavevector and taking $\epsilon_k = 1$ such that $\bar{\eta}_k = \eta_{0,exp}/2\epsilon_0$.

2. DERIVATION OF SEMIANALYTICAL MODEL

We start with the Landau-Lifshitz equation

$$\dot{\mathbf{m}} = -\gamma(\mathbf{m} \times \mathbf{H}_{\text{eff}}), \quad (11)$$

$$\mathbf{H}_{\text{eff}} = \mathbf{H}_0 + \mathbf{h}_a(\mathbf{t}) + \mathbf{h}_{\text{ex}} + \mathbf{h}_d \quad (12)$$

where \mathbf{m} is the unit vector of the magnetization, $\gamma=17.7$ MHz/Oe is the gyromagnetic ratio, \mathbf{H}_{eff} is the effective magnetic field, \mathbf{H}_0 is the applied static field, $\mathbf{h}_a(\mathbf{t})$ is the applied microwave field, \mathbf{h}_{ex} is the exchange field, and \mathbf{h}_d is the demagnetization field. We want to

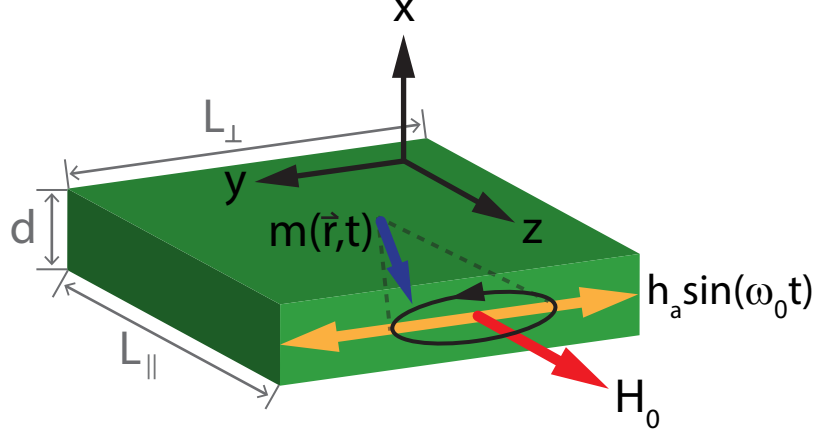


Fig. S1. Sample and field geometry. For the perpendicular pumping configuration, the static field H_0 is applied in-plane and perpendicular to the microwave field $h_a(t)$. H_0 saturates the static magnetization to M_s and sets its direction. h_a dynamically excites the magnetization, causing it to precess around the direction of its static component at an angle proportional to the magnon population. This precession is elliptical in thin films due to the dynamic demagnetization field.

re-express Eq. (11) in terms of the circular magnon modes $a_{\mathbf{k}}, a_{-\mathbf{k}}^*$, where [2]

$$\begin{aligned}
 m^+ &= m_x + im_y = \sum_{\mathbf{k}} a_{\mathbf{k}} e^{i\mathbf{k}\cdot\mathbf{r}} \delta, \\
 m^- &= m_x - im_y = \sum_{\mathbf{k}} a_{-\mathbf{k}}^* e^{i\mathbf{k}\cdot\mathbf{r}} \delta, \\
 \delta &= \frac{\Delta k_{\parallel} \Delta k_{\perp}}{(2\pi)^2}, \\
 \Delta k_{\parallel, \perp} &= \pi / L_{\parallel, \perp}.
 \end{aligned} \tag{13}$$

The summations are over all available in-plane wavevectors $\mathbf{k} = (k_{\parallel}, k_{\perp})$, where k_{\parallel}, k_{\perp} are the wavevector components parallel and perpendicular to the static magnetization direction, respectively. $\Delta k_{\parallel}, \Delta k_{\perp}$ are the magnon mode spacings parallel and perpendicular to the static magnetization direction. From Eq. (11), defining $\omega_i = \gamma H_{eff, i}$ and $\tilde{D} = \gamma D$ (with $D = 0.48 \text{ Oe } \mu\text{m}^2$ being the exchange stiffness) yields

$$\begin{aligned}
 \dot{\mathbf{m}}_{\mathbf{x}} &= m_z \omega_y - m_y \omega_z, \\
 \dot{\mathbf{m}}_{\mathbf{y}} &= m_x \omega_z - m_z \omega_x,
 \end{aligned} \tag{14}$$

where

$$\begin{aligned}
\omega_x &= \gamma(h_{ex,x} - h_{d,x}) = \tilde{D}\nabla^2 m_x - \omega_{d,x}, \\
\omega_y &= \gamma(h_{ex,y} - h_{d,y} + h_a(t)) = \tilde{D}\nabla^2 m_y - \omega_{d,y} + \omega_a(t), \\
\omega_z &= \gamma(h_{ex,z} - h_{d,z} + H_0) = \tilde{D}\nabla^2 m_z - \omega_{d,z} + \omega_H.
\end{aligned} \tag{15}$$

The demagnetization terms take the form [3], where d is the film thickness,

$$\begin{aligned}
\begin{pmatrix} \omega_{d,x} \\ \omega_{d,y} \\ \omega_{d,z} \end{pmatrix} &= 4\pi\gamma M_s \delta \sum_{\mathbf{k}} \begin{pmatrix} (1 - G_{\mathbf{k}}) & 0 & 0 \\ 0 & G_{\mathbf{k}} \frac{k_y^2}{k^2} & G_{\mathbf{k}} \frac{k_y k_z}{k^2} \\ 0 & G_{\mathbf{k}} \frac{k_y k_z}{k^2} & G_{\mathbf{k}} \frac{k_z^2}{k^2} \end{pmatrix} \begin{pmatrix} m_{\mathbf{k},x} \\ m_{\mathbf{k},y} \\ m_{\mathbf{k},z} \end{pmatrix}, \\
G_{\mathbf{k}} &= 1 - \frac{1 - e^{-kd}}{kd}, \\
m_{\mathbf{k},x} &= \frac{a_{\mathbf{k}} + a_{-\mathbf{k}}^*}{2} e^{i\mathbf{k}\cdot\mathbf{r}}, \\
m_{\mathbf{k},y} &= \frac{a_{\mathbf{k}} - a_{-\mathbf{k}}^*}{2i} e^{i\mathbf{k}\cdot\mathbf{r}}, \\
m_{\mathbf{k},z} &= 0.
\end{aligned} \tag{16}$$

We define $m_{\mathbf{k},z} = 0$ due to only taking the zeroth order term in the expansion $m_z = 1 - \frac{1}{2} \sum_{\mathbf{k},\mathbf{k}'} a_{\mathbf{k}'} a_{\mathbf{k}'-\mathbf{k}}^* e^{i\mathbf{k}\cdot\mathbf{r}}$, such that $m_z = 1$. As such, $m_{\mathbf{k},z}$ corresponds to the Kronecker delta $\delta_{\mathbf{k},0}$. However, the matrix elements vanish at $\mathbf{k} = 0$ such that the Kronecker delta can be neglected.

Next, due to its spatial homogeneity, we approximate the microwave field to only couple to the $\mathbf{k} = 0$ mode and solve for $\dot{m}^+ = \dot{m}_x + i\dot{m}_y = \sum_{\mathbf{k}} \dot{a}_{\mathbf{k}} e^{i\mathbf{k}\cdot\mathbf{r}} \delta$. Equating the coefficients of $e^{i\mathbf{k}\cdot\mathbf{r}}$ on each side yields the equations of motion for the circularly-precessing magnon modes. We only consider the equations of motion of the circular FMR magnon mode a_0 and the half-frequency ($f_0/2$) magnon modes $a_{\mathbf{k}_i}$. We have neglected all other modes because, barring higher-order interactions, they are not excited in the first order Suhl instability. The equations of motion of $a_0, a_{\mathbf{k}_i}$ are found to be:

$$\dot{a}_{\mathbf{k}_i} = i(A_{\mathbf{k}_i}a_{\mathbf{k}_i} + B_{\mathbf{k}_i}a_{-\mathbf{k}_i}^*) - a_0\phi_{\mathbf{k}_i}(a_{\mathbf{k}_i} - a_{-\mathbf{k}_i}^*), \quad (17)$$

$$\dot{a}_0 = i(A_0a_0 + B_0a_0^*) - \sum_{i=1}^{N_k} a_{\mathbf{k}_i}\phi_{-\mathbf{k}_i}(a_{-\mathbf{k}_i} - a_{-\mathbf{k}_i}^*) + \omega_a(t), \quad (18)$$

$$A_{\mathbf{k}} = \omega_H + \tilde{D}k^2 + 2\pi\gamma M_s[1 - G_{\mathbf{k}} + G_{\mathbf{k}}\frac{k_y^2}{k^2}], \quad (19)$$

$$B_{\mathbf{k}} = 2\pi\gamma M_s[1 - G_{\mathbf{k}} - G_{\mathbf{k}}\frac{k_y^2}{k^2}], \quad (20)$$

$$\phi_{\mathbf{k}} = 2\pi\gamma M_s\delta G_{\mathbf{k}}\frac{k_y k_z}{k^2} = 2\pi\gamma M_s\delta G_{\mathbf{k}}\sin\theta_{\mathbf{k}}\cos\theta_{\mathbf{k}}. \quad (21)$$

Note that we only kept terms up to second order in a , neglecting higher-order interactions. The $A_{\mathbf{k}}$ and $B_{\mathbf{k}}$ terms correspond to the magnon's angular frequency $\omega_{\mathbf{k}_i}$ such that $\omega_{\mathbf{k}_i} = \sqrt{A_{\mathbf{k}_i}^2 - B_{\mathbf{k}_i}^2}$. $\phi_{\mathbf{k}}$ is the coupling strength between the circular FMR magnons and the circular magnons at $f_0/2$; the second-order terms, proportional to $\phi_{\mathbf{k}}$, are the three-magnon scattering terms. The summation in Eq. (18) captures three-magnon scattering of a_0 to the N_k magnon modes in the frequency range $(\omega_0/2 - \eta_{\mathbf{k}}) < \omega_{\mathbf{k}_i} < (\omega_0/2 + \eta_{\mathbf{k}})$. $\eta_{\mathbf{k}}$ is the relaxation rate of the $f_0/2$ modes, whose ellipticity is negligible. The $\omega_a(t)$ term corresponds to the driving from the microwave field.

Next, we perform a Bogoliubov transformation [4] to the magnon eigenmodes; as the dynamic demagnetization field in thin films leads to elliptical magnetization precession, the eigenmodes correspond to the elliptically-precessing magnon modes $b_{\mathbf{k}}, b_{-\mathbf{k}}^*$:

$$\begin{aligned} \begin{pmatrix} b_{\mathbf{k}} \\ b_{-\mathbf{k}}^* \end{pmatrix} &= \begin{pmatrix} \lambda_{\mathbf{k}} & \mu_{\mathbf{k}} \\ \mu_{\mathbf{k}} & \lambda_{\mathbf{k}} \end{pmatrix} \begin{pmatrix} a_{\mathbf{k}} \\ a_{-\mathbf{k}}^* \end{pmatrix}; \\ \begin{pmatrix} a_{\mathbf{k}} \\ a_{-\mathbf{k}}^* \end{pmatrix} &= \begin{pmatrix} \lambda_{\mathbf{k}} & -\mu_{\mathbf{k}} \\ -\mu_{\mathbf{k}} & \lambda_{\mathbf{k}} \end{pmatrix} \begin{pmatrix} b_{\mathbf{k}} \\ b_{-\mathbf{k}}^* \end{pmatrix}, \\ \lambda_{\mathbf{k}} &= \cosh(\xi_{\mathbf{k}}), \\ \mu_{\mathbf{k}} &= -\sinh(\xi_{\mathbf{k}}), \\ \tanh(2\xi_{\mathbf{k}}) &= B_{\mathbf{k}}/A_{\mathbf{k}}. \end{aligned} \quad (22)$$

To perform the Bogoliubov transformation of a given $f_0/2$ mode $a_{\mathbf{k}_i}$, we express its equations

of motion in matrix form as

$$\begin{pmatrix} \dot{a}_{\mathbf{k}_i} \\ \dot{a}_{-\mathbf{k}_i}^* \end{pmatrix} = (iL_{0,\mathbf{k}_i} + \phi_{\mathbf{k}_i}L_1) \begin{pmatrix} a_{\mathbf{k}_i} \\ a_{-\mathbf{k}_i}^* \end{pmatrix}, \quad (23)$$

$$L_{0,\mathbf{k}_i} = \begin{pmatrix} A_{\mathbf{k}_i} & B_{\mathbf{k}_i} \\ -B_{\mathbf{k}_i} & -A_{\mathbf{k}_i} \end{pmatrix}, \quad (24)$$

$$L_1 = \begin{pmatrix} -a_0 & a_0 \\ a_0^* & -a_0^* \end{pmatrix}. \quad (25)$$

Performing the Bogoliubov transformation of Eq. (23) yields

$$\begin{pmatrix} \dot{b}_{\mathbf{k}_i} \\ \dot{b}_{-\mathbf{k}_i}^* \end{pmatrix} = \left[i \begin{pmatrix} \omega_{\mathbf{k}_i} & 0 \\ 0 & -\omega_{\mathbf{k}_i} \end{pmatrix} + \phi_{\mathbf{k}_i}(\lambda_{\mathbf{k}_i} + \mu_{\mathbf{k}_i}) \begin{pmatrix} \mu_{\mathbf{k}_i}a_0^* - a_0\lambda_{\mathbf{k}_i} & \lambda_{\mathbf{k}_i}a_0 - \mu_{\mathbf{k}_i}a_0^* \\ \lambda_{\mathbf{k}_i}a_0^* - \mu_{\mathbf{k}_i}a_0 & \mu_{\mathbf{k}_i}a_0 - \lambda_{\mathbf{k}_i}a_0^* \end{pmatrix} \right] \begin{pmatrix} b_{\mathbf{k}_i} \\ b_{-\mathbf{k}_i}^* \end{pmatrix}. \quad (26)$$

In the second matrix on the right-hand side, we substitute a_0, a_0^* in terms of b_0, b_0^* . Given their frequencies $b_0 \propto e^{i\omega_0 t}, b_0^* \propto e^{-i\omega_0 t}$, we only retain the terms with the same frequency as that on the left-hand side $b_{\mathbf{k}_i} \propto e^{i\omega_0 t/2}, b_{-\mathbf{k}_i}^* \propto e^{-i\omega_0 t/2}$. Doing so, we obtain

$$\dot{b}_{\mathbf{k}_i} = i\omega_{\mathbf{k}_i}b_{\mathbf{k}_i} + \zeta_{\mathbf{k}_i}b_0b_{-\mathbf{k}_i}^*, \quad (27)$$

$$\zeta_{\mathbf{k}_i} = (\lambda_{\mathbf{k}_i} + \mu_{\mathbf{k}_i})(\lambda_{\mathbf{k}_i}\lambda_0 + \mu_{\mathbf{k}_i}\mu_0)\phi_{\mathbf{k}_i}. \quad (28)$$

$\zeta_{\mathbf{k}_i}$ is the coupling strength between the elliptical FMR mode b_0 and the given elliptical $f_0/2$ mode $b_{\mathbf{k}_i}$. Note that, as an approximation, we have set the angular frequencies $\omega_{\mathbf{k}_i}$ of all magnon modes in the frequency range $(\omega_0/2 - \eta_{\mathbf{k}}) < \omega_{\mathbf{k}_i} < (\omega_0/2 + \eta_{\mathbf{k}})$ to be equal to $\omega_{\mathbf{k}_i} = \omega_0/2$. This approximation is reasonable for low-damping materials such as YIG, where $\eta_{\mathbf{k}} \ll \omega_0/2$. Repeating these steps for the Bogoliubov transformation for \dot{a}_0 yields

$$\dot{b}_0 = i\omega_0b_0 - \sum_{i=1}^{N_{\mathbf{k}}} \zeta_{\mathbf{k}_i}b_{\mathbf{k}_i}^2 + (\lambda_0 + \mu_0)\omega_a(t), \quad (29)$$

where the summation is over all $N_{\mathbf{k}}$ elliptical magnon modes $b_{\mathbf{k}_i}$ in the frequency range $(\omega_0/2 - \eta_{\mathbf{k}}) < \omega_{\mathbf{k}_i} < (\omega_0/2 + \eta_{\mathbf{k}})$.

Next, we account for linear magnon damping by adding the term $-\eta_{\mathbf{k}_i}b_{\mathbf{k}_i}$, where

$$\eta_{\mathbf{k}_i} = \omega_{\mathbf{k}_i}\alpha\epsilon_{\mathbf{k}_i} = \omega_{\mathbf{k}_i}\alpha \frac{1}{\gamma} \left(\frac{\partial\omega}{\partial H} \right) \Big|_{\mathbf{k}_i, H_0}. \quad (30)$$

$\eta_{\mathbf{k}_i}$ corresponds to the relaxation rate of magnon mode $b_{\mathbf{k}_i}$, α is the measured Gilbert damping constant, and $\epsilon_{\mathbf{k}_i}$ is the ellipticity factor of the magnon mode $b_{\mathbf{k}_i}$.

We take the driving term to be sinusoidal, substituting $\omega_a = \frac{\gamma h_a}{2} e^{-i\pi/2} (e^{i\omega_0 t} + e^{-i\omega_0 t})$ into the equation of motion. We only keep its term proportional to $e^{i\omega_0 t}$ because that is the term that matches the FMR frequency ω_0 . This yields the elliptical magnon modes' equations of motion:

$$\dot{b}_0 = (i\omega_0 - \eta_0)b_0 - \sum_{i=1}^{N_k} \zeta_{\mathbf{k}_i} b_{\mathbf{k}_i}^2 + \nu h_a e^{i(\omega_0 t - \pi/2)}, \quad (31)$$

$$\dot{b}_{\mathbf{k}_i} = (i\omega_k - \eta_{\mathbf{k}_i})b_{\mathbf{k}_i} + \zeta_{\mathbf{k}_i} b_0 b_{-\mathbf{k}_i}^*, \quad (32)$$

$$\nu = \gamma(\lambda_0 + \mu_0)/2. \quad (33)$$

ν is the coupling of b_0 to the microwave field amplitude h_a . This system of $(N_k + 1)$ equations can be simplified by taking $\zeta_{\mathbf{k}_i} = \bar{\zeta}$ and $\eta_{\mathbf{k}_i} = \bar{\eta}_k$, their average values over the N_k magnon modes. We also set $b_{-\mathbf{k}_i}^* = b_{\mathbf{k}_i}^*$, as the splitting and confluence processes affect each mode equally. This causes the equation of motion for each mode $b_{\mathbf{k}_i}$ to be equivalent. We also take each mode's initial value, its thermal amplitude, to be equivalent (which is a good approximation, as $\eta_{\mathbf{k}_i} \ll \omega_{\mathbf{k}_i}$). Making each $b_{\mathbf{k}_i}$ mode equivalent in this way reduces their N_k equations of motion to a single equation of motion of an effective $f_0/2$ mode b_k . This simplifies our model to the two equations of motion:

$$\dot{b}_0 = (i\omega_0 - \eta_0)b_0 - N_k \bar{\zeta} b_k^2 + \nu h_a e^{i(\omega_0 t - \pi/2)}, \quad (34)$$

$$\dot{b}_k = (i\omega_k - \bar{\eta}_k)b_k + \bar{\zeta} b_k^* b_0. \quad (35)$$

b_0 is the response of the elliptical FMR mode and b_k is the response of the effective $f_0/2$ mode. Note that these are the same equations as those stated in Eqs. (1,2) of the main text.

3. DERIVATION OF THERMAL MAGNON AMPLITUDE

To numerically solve our model we must calculate the magnon mode's initial values, which correspond to their thermal amplitudes. This is done by bridging our semiclassical magnon modes $b_{\mathbf{k},c}, b_{-\mathbf{k},c}^*$ with their quantum-mechanical counterparts $b_{\mathbf{k},q}, b_{-\mathbf{k},q}^\dagger$ [4], whose thermal amplitudes are given by the Bose-Einstein distribution function. Ref. [4], for small magnon

mode amplitudes, provides the approximation

$$M^+ \approx B \sum_{\mathbf{k}} (\lambda_{\mathbf{k}} b_{\mathbf{k},q} + \mu_{\mathbf{k}} b_{-\mathbf{k},q}^\dagger) e^{i\mathbf{k}\cdot\mathbf{r}} \delta; \quad (36)$$

$$B = \sqrt{2\hbar\gamma M_s/V}, \quad (37)$$

$$\delta = \frac{\Delta k_{\parallel} \Delta k_{\perp}}{(2\pi)^2}. \quad (38)$$

$V = L_{\parallel} L_{\perp} d$ is the sample size in units of cm^3 , and $\Delta k_{\parallel}, \Delta k_{\perp} = \pi/L_{\parallel,\perp}$ are the magnon mode spacings parallel and perpendicular to the magnetization, respectively. For our semiclassical formulation,

$$M^+ = M_s m^+ = M_s \sum_{\mathbf{k}} (\lambda_{\mathbf{k}} b_{\mathbf{k},c} + \mu_{\mathbf{k}} b_{-\mathbf{k},c}^*) e^{i\mathbf{k}\cdot\mathbf{r}} \delta. \quad (39)$$

Equating the two forms of M^+ , we find that $b_{\mathbf{k},c} = \frac{B}{M_s} b_{\mathbf{k},q}$, yielding the thermal amplitude of the semiclassical magnon modes:

$$(b_{\mathbf{k},c})_{th} = \frac{B}{M_s} (b_{\mathbf{k},q})_{th} = \sqrt{\frac{2\hbar\gamma f_{BE}(\mathbf{k})}{M_s V}}, \quad (40)$$

$$f_{BE}(\mathbf{k}) = (e^{\hbar f_{\mathbf{k}}/k_B T} - 1)^{-1}. \quad (41)$$

Note that we take $(b_{\mathbf{k},c})_{th} = (c_{\mathbf{k},c})_{th}$.

4. COMPUTATIONAL METHODS

A. Numerical solutions of model

For the numerical solutions to our model, the relevant magnon modes are found through calculating the dispersion only for positive $(k_{\parallel}, k_{\perp})$, where \parallel and \perp correspond to the magnon wavevector component parallel and perpendicular to the static magnetization direction. This prevents double-counting with the modes at negative $(k_{\parallel}, k_{\perp})$, and the modes in the other quadrants are negligible due to having a negative coupling strength [as seen through the coupling strength being proportional to $\sin(\theta_{\mathbf{k}_i})\cos(\theta_{\mathbf{k}_i})$ in Eq. (21) and evidenced in the simulation results of Ref. [5]].

For the determination of the relevant magnon modes and the numerical solving of their equations of motion, we utilize the value of η_0 measured in the experiment, which we define

as $\eta_{0,exp}$. We measure $c_0(t)$ at several powers in the linear regime and fit the time-dependence to the standard form $c_0(t) \propto (1 - e^{-\eta_0 t})$, yielding the fitted value of η_0 for each power. $\eta_{0,exp}$ corresponds to the average of these fitted values of η_0 . From the definition $\eta_i = \omega_i \alpha \epsilon_i$, we can calculate the associated Gilbert damping constant α_{exp} for a given FMR frequency f_0 and the associated ellipticity factor ϵ_0 . α_{exp} is the value used to calculate the associated values of $\eta_{\mathbf{k}_i}$ to obtain $\bar{\eta}_k$.

We take the $f_0/2$ magnon modes in our calculated dispersion to be those in the frequency range $\omega_0/2 - \eta_k < \omega < \omega_0/2 + \eta_k$, where we approximate negligible ellipticity such that $\eta_k = \omega_0 \alpha_{exp}/2$. The number of modes in this range is our calculated value of N_k , and we calculate their individual coupling strengths and their relaxation rates $\zeta_{\mathbf{k}_i}, \eta_{\mathbf{k}_i}$ to obtain the average values over these modes $\bar{\zeta}, \bar{\eta}_k$.

For numerically solving our model, we need to utilize values of h_a such that the relative excitation h_a/h_S is consistent with that in the experiment and simulations; h_S is the threshold value of h_a for the instability. Our linearization of the equations of motion of c_0, c_k provides the analytical value $h_S = \eta_0 \bar{\eta}_k / \nu \bar{\zeta}$ (see Sec. 6), which we find to be valid for the numerical solving of c_0, c_k . However, for numerically solving b_0, b_k , this value of h_S is found to no longer be valid, potentially due to the influence of the phase degree of freedom on the onset of the instability. By numerically solving for b_0, b_k with trial values of h_a to find h_S , we find that the associated value of h_S increases by a factor of approximately 5.6, or 15 dB in power.

Lastly, to numerically solve our model, we need to calculate the initial values of b_i, c_i . We take these to correspond to their thermal amplitudes, which are calculated through the Bose-Einstein distribution. To do so, we connect our semiclassical formulation with the quantum-mechanical formulation in Ref. [4] (see Sec. 3). With these calculated values for the parameters and initial values, we numerically solved the equations of motion through the ode45 function in MATLAB. For the derivation of our model, see Sec. 2.

B. Micromagnetic simulations

Micromagnetic simulations were performed using the Landau-Lifshitz-Gilbert (LLG) equation [6, 7]

$$\dot{\mathbf{m}} = -\gamma \mathbf{m} \times (\mathbf{H}_{\text{eff}} + \boldsymbol{\xi}(T)) + \alpha \mathbf{m} \times \dot{\mathbf{m}}, \quad (42)$$

$$\mathbf{H}_{\text{eff}} = \mathbf{H}_0 + \mathbf{h}_a(t) + \mathbf{h}_{\text{ex}} + \mathbf{h}_d, \quad (43)$$

where $\mathbf{m}(\mathbf{r}, t)$ is the unit vector of the local magnetization and $\gamma = 17.7$ MHz/Oe is the gyromagnetic ratio. \mathbf{H}_{eff} is the effective field including the in-plane static field \mathbf{H}_0 , the applied microwave field $\mathbf{h}_a(t)$, the exchange field \mathbf{h}_{ex} , and the demagnetization field \mathbf{h}_d . $\boldsymbol{\xi}(T)$ is the thermal fluctuation field and α is the Gilbert damping constant. $\boldsymbol{\xi}(T)$ is dependent on the temperature T [8, 9] and corresponds to a white-noise field whose amplitude ξ is determined by the equation

$$\xi(T) = \sqrt{\frac{2k_B T \alpha}{\gamma V dt M_s}}. \quad (44)$$

k_B is the Boltzmann constant, V is the cell volume in the simulation, dt is the utilized time increment, and M_s is the saturation magnetization.

The Cartesian coordinate system and magnetic field orientations are the same as those shown in Fig. S1 in Sec. 2. As the microwave pumping frequency f_0 is ~ 1 GHz, the wavelength of the microwaves is ~ 1 cm. Compared to our simulated system of ~ 1 mm lateral size, the microwave field can be treated as a uniform ac magnetic field oscillating at the frequency f_0 .

For our sample material, yttrium iron garnet, we use the following parameters for the simulation: the gyromagnetic ratio $\gamma=17.7$ MHz/Oe, the exchange constant $A=3.5 \times 10^{-7}$ erg/cm, and the saturation magnetization $M_s=130$ emu/cm³. Note that, to improve computational efficiency via reduction of the instability's timescales, we utilized an inflated value of the Gilbert damping constant for the simulations, setting $\alpha_{sim} = 0.005$. This also inflates the corresponding value of h_{osc} , necessitating the normalization to h_{osc} in our definition $\tilde{h} = (h_a - h_{osc})/h_{osc}$ in the main text.

A custom parallel-computing code based on CUDA [10] is used to optimize the computational performance. The lateral size of the system under study is $30 \mu\text{m} \times 30 \mu\text{m}$, and the thickness is $3 \mu\text{m}$. This system is discretized into cells with the dimensions $100 \text{ nm} \times 100 \text{ nm} \times 3 \mu\text{m}$. For each timestep $dt = 50$ fs, the simulation numerically solves the LLG

equation for each cell to compute its magnetization. From this time- and space-resolved data, we can calculate the time-resolved magnon mode amplitudes $c(\mathbf{k}, t)$, as done in ref. [5].

As the timescales of the instability are inversely proportional to α , the inflation of α necessitates re-scaling of the times in the simulation. As such, to enable direct comparison of our simulations with both our experiment and the numerical solutions to our model, we re-scale its time values by the factor $\alpha_{sim}/\alpha_{exp}$, where α_{exp} is calculated as described in the previous subsection.

5. DATA AT 2.5 GHz FMR FREQUENCY

In Fig. S2, the top row ($f_0 = 1.5$ GHz) is the same data as that in Fig. 2 of the main text, with the corresponding data at $f_0 = 2.5$ GHz shown in the bottom row. For a given FMR frequency, each approach shows strong qualitative agreement for a given relative power P_a/P_S . An inset of the highest-power experimental data at each frequency is provided to show the crossings of c_0 through zero, corresponding to 180° phase shifts of b_0 .

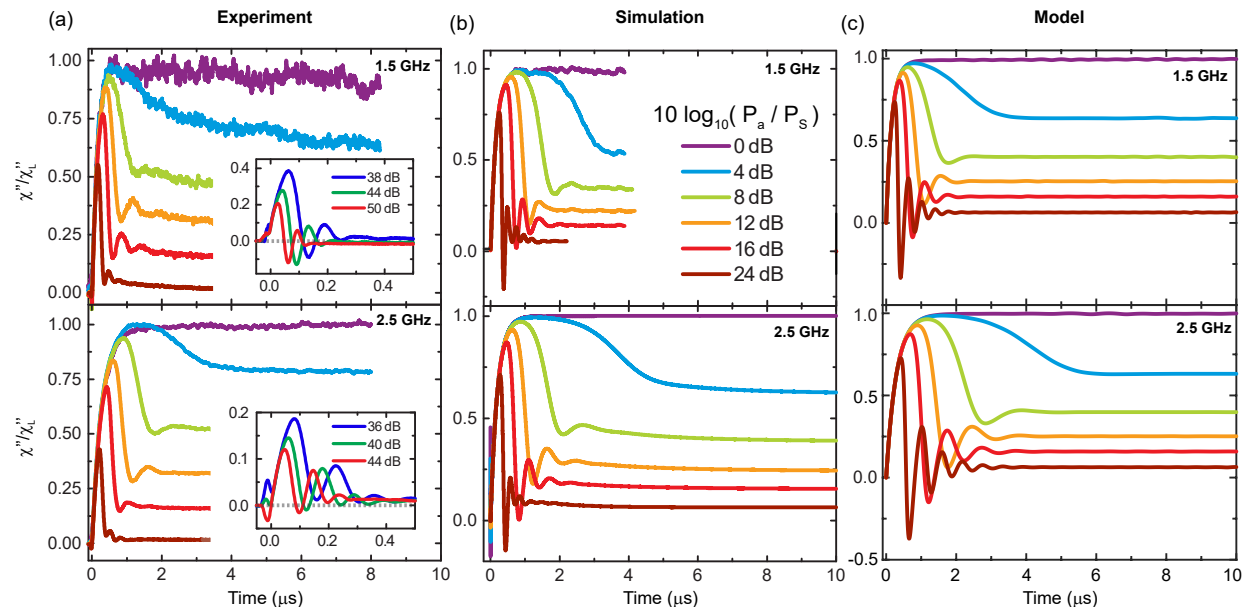


FIG. S2 Full comparison of the instability's nonequilibrium behavior from (a) the experiment, (b) the simulations, and (c) the numerical solutions to Eqs. (3,4). The top row ($f_0 = 1.5$ GHz) is the same data as in Fig. 2 of the main text. The corresponding data at $f_0 = 2.5$ GHz is shown in the bottom row.

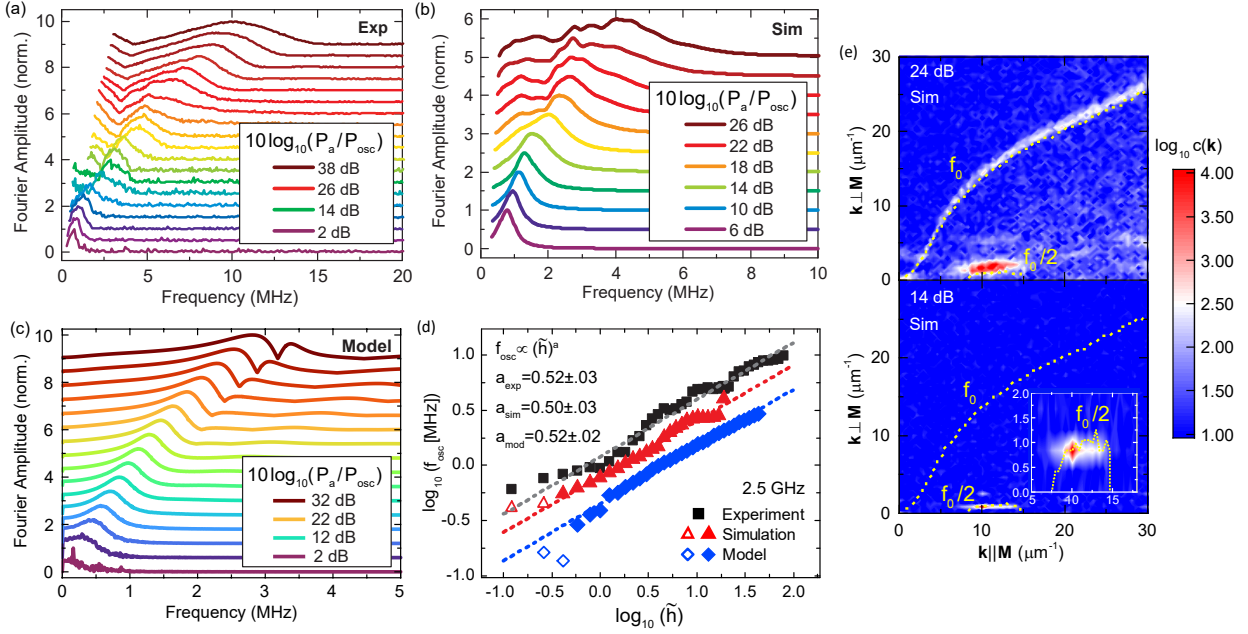


FIG. S3 Oscillation analysis for $f_0 = 2.5$ GHz. (a-c) Normalized and offset frequency spectra of the oscillations in (a) the experiment, (b) the micromagnetic simulations, and (c) the numerical solutions to Eqs. (3,4) in the main text. (d) The scaling of the oscillation frequency f_{osc} for each approach. The filled symbols indicate the fitted region, where quantitative agreement of the scaling with our linearized model is observed. (e) The simulated steady-state magnon amplitudes $c(\mathbf{k})$ for powers 14 dB (bottom) and 24 dB (top) above the oscillation threshold.

Figure S3 is the same layout as Fig. 3 in the main text, but with the data being at $f_0 = 2.5$ GHz and the inclusion of the oscillations' frequency spectra from the model's numerical solutions. In these numerical solutions, the lopsidedness of the transient behavior at high powers [see Fig. S2(c)] leads to a distortion in their frequency spectra [Fig. S3(c)]. As such, we isolate the analysis of the numerical solutions' frequency scaling to powers below which this distortion dominates the spectra. As at $f_0 = 1.5$ GHz, we observe quantitative agreement of the scaling of f_{osc} with that predicted by our linearized model over several orders of magnitude in microwave power. Note that, in Fig. S3(d), there is a 1 dB increment in power between points.

In the experiment and simulations, as observed for $f_0 = 1.5$ GHz, the oscillations' frequency spectra broadens for relative powers above approximately 14 dB [Figs. S3(a,b)]. Fig. S3(e) shows, for the relative powers of 14 dB (minimal broadening) and 24 dB (pronounced broadening), the steady-state magnon amplitudes $c(\mathbf{k})$ from simulations. As observed at

$f_0 = 1.5$ GHz in the main text, this broadening corresponds to a transition from isolated excitation of the strongest-coupled $f_0/2$ modes to excitation of many weaker-coupled $f_0/2$ modes. The excited modes at 25 dB exhibit a wider frequency distribution around $f_0/2$, which may cause the observed broadening. Recall that this transition is hypothesized to be four-magnon scattering from strongly- to weakly-coupled $f_0/2$ magnon pairs, conserving energy and momentum.

However, for $f_0 = 2.5$ GHz, there is additional magnon excitation along the f_0 contour (top panel). Similarly, the most straightforward mechanism for this excitation is four-magnon scattering of two FMR magnons to two f_0 magnons of equal and opposite wavevectors, which conserves energy and momentum. This four-magnon scattering process corresponds to the second order Suhl instability, which is the relevant instability when magnon modes at $f_0/2$ are unavailable.

6. DERIVATION OF DIFFERENT REGIMES AND THE OSCILLATION SCALING

In order to analyze the oscillatory regime, we linearize Eqs. (3,4) in the main text. These equations are the elliptical magnon amplitudes' equations of motion for the weakly nonlinear case, where phase shifts are negligible:

$$\dot{c}_0 = -\eta_0 c_0 - N_k \bar{\zeta} c_k^2 + \nu h_a, \quad (45)$$

$$\dot{c}_k = -\bar{\eta}_k c_k + \bar{\zeta} c_k c_0. \quad (46)$$

We linearize these equations by examining around their fixed points, which are the values $(c_{0,f}, c_{k,f})$ such that $\dot{c}_0 = \dot{c}_k = 0$. This allows us to treat the second-order time-varying terms as negligible, converting the equations of motion into a linear form.

A. Linearization of the equations of motion

To examine the equations of motion near a fixed point, we define

$$\begin{pmatrix} c_0(t) \\ c_k(t) \end{pmatrix} = \begin{pmatrix} c_{0,f} \\ c_{k,f} \end{pmatrix} + \begin{pmatrix} U(t) \\ V(t) \end{pmatrix}, \quad U(t), V(t) \ll 1. \quad (47)$$

Given these definitions, Taylor expanding \dot{c}_0, \dot{c}_k about $(c_{0,f}, c_{k,f})$ with the Jacobian

$$J|_{c_{0,f}, c_{k,f}} = \begin{pmatrix} \partial\dot{c}_0/\partial c_0 & \partial\dot{c}_0/\partial c_k \\ \partial\dot{c}_k/\partial c_0 & \partial\dot{c}_k/\partial c_k \end{pmatrix} \Big|_{c_{0,f}, c_{k,f}} = \begin{pmatrix} -\eta_0 & -2N_k\bar{\zeta}c_{k,f} \\ \bar{\zeta}c_{k,f} & -\bar{\eta}_k + \bar{\zeta}c_{0,f} \end{pmatrix} \quad (48)$$

yields

$$\begin{pmatrix} \dot{c}_0 \\ \dot{c}_k \end{pmatrix} = \begin{pmatrix} \dot{U} \\ \dot{V} \end{pmatrix} \approx \begin{pmatrix} -\eta_0 & -2N_k\bar{\zeta}c_{k,f} \\ \bar{\zeta}c_{k,f} & -\bar{\eta}_k + \bar{\zeta}c_{0,f} \end{pmatrix} \begin{pmatrix} U \\ V \end{pmatrix}. \quad (49)$$

We then impose the form

$$\begin{pmatrix} U \\ V \end{pmatrix} = \begin{pmatrix} ae^{\lambda t} \\ be^{\lambda t} \end{pmatrix} \quad (50)$$

to generate the eigenvalue equation

$$\lambda \begin{pmatrix} U \\ V \end{pmatrix} = \begin{pmatrix} -\eta_0 & -2N_k\bar{\zeta}c_{k,f} \\ \bar{\zeta}c_{k,f} & -\bar{\eta}_k + \bar{\zeta}c_{0,f} \end{pmatrix} \begin{pmatrix} U \\ V \end{pmatrix}, \quad (51)$$

with solutions of λ such that

$$\det(J|_{c_{0,f}, c_{k,f}} - \lambda I) = 0. \quad (52)$$

Solving this equation provides the following solution for the two possible values of λ :

$$\lambda_{\pm} = \frac{-\rho \pm \sqrt{\rho^2 - 4\sigma}}{2} \quad (53)$$

$$\rho = \eta_0 + \bar{\eta}_k - \bar{\zeta}c_{0,f} \quad (54)$$

$$\sigma = \eta_0\bar{\eta}_k + 2N_k(\bar{\zeta}c_{k,f})^2 - \eta_0\bar{\zeta}c_{0,f}. \quad (55)$$

The above is still general, with insertion of the fixed point values $(c_{0,f}, c_{k,f})$ for a given regime providing its associated behavior.

B. Linear regime

The fixed point for the linear regime corresponds to

$$(c_{0,f}, c_{k,f}) = (\nu h_a / \eta_0, 0). \quad (56)$$

Near this fixed point, one can approximate $c_k^2 \approx 0$ such that

$$\dot{c}_0 = -\eta_0 c_0 + \nu h_a. \quad (57)$$

Including a constant in the solution of the above equation's homogeneous form and applying the boundary conditions $c_0(0) = 0, c_0(\infty) = \nu h_a / \eta_0$ yields the analytical solution for $c_0(t)$, which has the standard time-dependence in the linear regime:

$$c_0(t) = \frac{\nu h_a}{\eta_0} (1 - e^{-\eta_0 t}). \quad (58)$$

We find, upon fitting this equation's time-dependence to the linear FMR behavior in simulations, that the fitted value of η_0 closely aligns with its expected value $\eta_0 = \omega_0 \alpha_{sim} \epsilon_0$. ω_0 is the FMR angular frequency, α_{sim} is the Gilbert damping constant used in the simulation, and ϵ_0 is the calculated ellipticity factor of the FMR mode. Specifically, the discrepancy between the fitted and defined value of η_0 is $< 0.5\%$ at 2.5 GHz, and is $< 5\%$ at 1.5 GHz. The above time-dependence for $c_0(t)$ is that used in fitting the experimental data in the linear regime, yielding the experimental value of η_0 used in the numerical solving of our model.

Furthermore, inserting the linear regime's fixed point into Eq. (53) yields the Suhl instability's threshold microwave field amplitude h_S , the value of h_a such that λ_+ becomes positive:

$$h_S = \eta_0 \bar{\eta}_k / \nu \bar{\zeta}. \quad (59)$$

C. Nonlinear regime

The nonlinear regime's fixed point, for which $c_{k,f}$ has a finite value, corresponds to

$$(c_{0,f}, c_{k,f}) = \left(\frac{\bar{\eta}_k}{\bar{\zeta}}, \sqrt{\frac{\nu h_a - \eta_0 \bar{\eta}_k / \bar{\zeta}}{N_k \bar{\zeta}}} \right). \quad (60)$$

Through the definition of h_S , Eq. (60) can be re-expressed in terms of h_S . This yields the power-dependence of the steady-state value of c_k , $c_k \propto \sqrt{h_a - h_S}$, stated in the main text:

$$c_{k,f} = \sqrt{\frac{\nu}{N_k \bar{\zeta}} (h_a - h_S)}. \quad (61)$$

Solving for λ_{\pm} with the fixed point values in the nonlinear regime yields the eigenvalues

$$\lambda_{\pm} = -\frac{\eta_0}{2} \pm \sqrt{\eta_0^2 / 4 - 2 \bar{\zeta} \nu (h_a - h_S)}. \quad (62)$$

Note that, as h_a is increased past h_S , λ_+ becomes negative such that the nonlinear fixed point becomes stable. Simultaneously, the linear regime's fixed point becomes unstable.

This corresponds to the linear and nonlinear regimes' fixed points exchanging stability as h_a is swept through h_S , which is defined as a transcritical bifurcation.

As h_a is increased further, past the critical value h_{osc} , it causes the radicand in Eq. (62) to cross through zero and become negative. This corresponds to the nonlinear regime's fixed point transitioning from a stable node (λ_{\pm} being purely real with a negative value) to a stable spiral (λ_{\pm} being complex with a negative real component). This marks the transition to the nonlinear oscillatory regime. Solving for the critical value of h_a that causes the radicand to vanish yields h_{osc} :

$$h_{osc} = h_S \left(1 + \frac{\eta_0}{8\bar{\eta}_k}\right). \quad (63)$$

This is the same form as the definition of h_{osc} stated in the main text. Re-expressing the radicand in terms of h_{osc} , we find

$$\lambda_{\pm} = -\eta_0/2 \pm i\omega_{osc}, \quad (64)$$

$$\omega_{osc} = 2\pi f_{osc} = \frac{\eta_0}{2} \sqrt{2\bar{\zeta}\nu(h_a - h_{osc})}. \quad (65)$$

This yields the definition of f_{osc} stated in the main text:

$$f_{osc} = \eta_0 \sqrt{\frac{\bar{\zeta}\nu}{8\pi^2}(h_a - h_{osc})}. \quad (66)$$

7. ANALYSIS OF OSCILLATIONS

The frequency spectra of the oscillations were obtained by doing a fast Fourier transform (FFT) of a window of data of $c_0(t)$. The utilized windows cover the time interval from t_{start} , just before the oscillations, to the end of the pulse [Fig. S4(a)]. Before performing the FFT, the window of data was symmetrized and had its average value subtracted to suppress DC contributions to the spectra [Fig. S4(b)]. In addition, for the FFT of the processed data window [Fig. S4(c)], an exclusion of the low-frequency Fourier amplitudes is introduced to better isolate the frequency spectra of the oscillations from DC artifacts. The window of this exclusion is incrementally increased at each power to offset the associated growth of the DC artifact. The oscillation frequency f_{osc} for a given power is defined as that of the largest Fourier amplitude and/or the visible center of the distribution [Fig. S4(c)]. The latter convention is prioritized in the few cases where the former convention provides visibly erroneous results for the characteristic oscillation frequency.

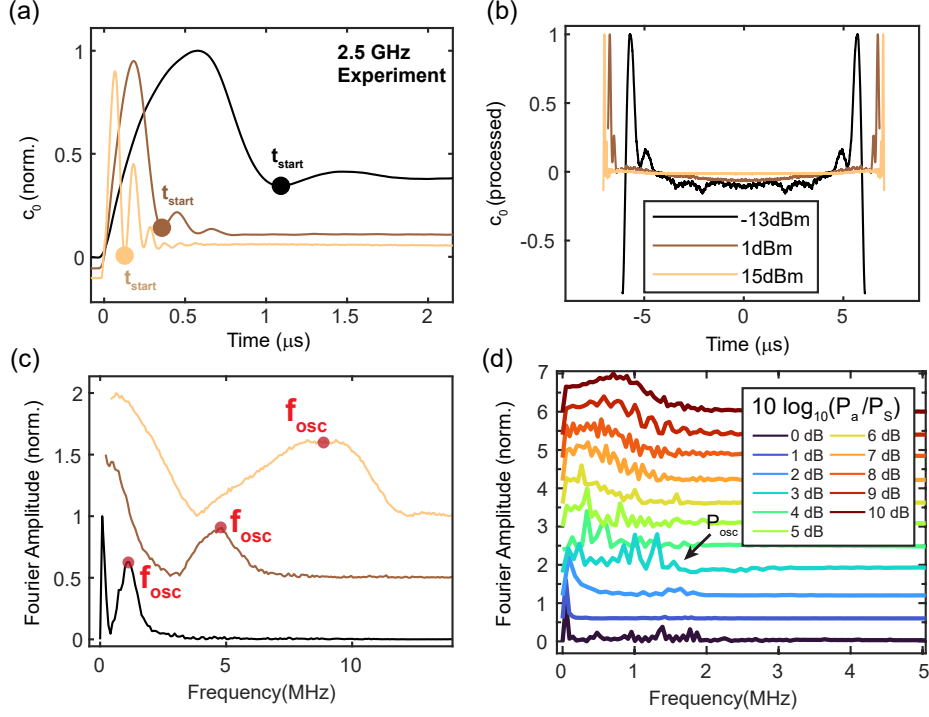


FIG. S4. Analysis of the oscillations. (a) Making the window for analyzing the oscillations. (b) Illustration of the processing of the signal. (c) The Fast Fourier Transforms of the processed data in (b) and the determination of their characteristic oscillation frequency f_{osc} . (d) Example of the determination of P_{osc} from these spectra.

From the oscillations' spectra, we estimate P_{osc} for each approach as the highest power for which no oscillation-induced structure in the spectra is observed. An example of this determination is shown in Fig. S4(d). The arisal of the oscillations corresponds to the arisal of the broad structure localized at low frequencies, as seen in the 4 dB data at ≈ 0.5 MHz.

For calculating the scaling of the oscillation frequency in the experiment, we need to convert both P_{osc} to h_{osc} and P_a to h_a in order to calculate the associated values of $\tilde{h} = (h_a - h_{osc})/h_{osc}$. The conversion factor β can be considered as $h = \beta\sqrt{P}$. However, given the normalized form of \tilde{h} , β will cancel between the numerator and denominator. This allows us to directly solve for \tilde{h} given the absolute powers of P_a and P_{osc} :

$$\tilde{h} = \frac{\sqrt{P_a} - \sqrt{P_{osc}}}{\sqrt{P_{osc}}}. \quad (67)$$

[1] Matesy web site, <https://matesy.de/en/products/materials/yig-films>.

- [2] H. Suhl, The theory of ferromagnetic resonance at high signal powers, *J. Phys. Chem. Solids* **1**, 209 (1957).
- [3] B. A. Kalinikos and A. N. Slavin, Theory of dipole-exchange spin wave spectrum for ferromagnetic films with mixed exchange boundary conditions, *J. Phys. C* **19**, 7013 (1986).
- [4] A. Y. Dobin and R. H. Victora, Intrinsic nonlinear ferromagnetic relaxation in thin metallic films, *Phys. Rev. Lett.* **90**, 167203 (2003).
- [5] T. Qu, P. A. Crowell, R. H. Victora, *et al.*, Nonlinear magnon scattering mechanism for microwave pumping in magnetic films, *IEEE Access* **8**, 216960 (2020).
- [6] Y.-H. Tang, N. Kioussis, A. Kalitsov, W. Butler, and R. Car, Influence of asymmetry on bias behavior of spin torque, *Phys. Rev. B* **81**, 054437 (2010).
- [7] N. A. Natekar, W.-H. Hsu, and R. H. Victora, Calculated dependence of FePt damping on external field magnitude and direction, *AIP Adv.* **7**, 056004 (2017).
- [8] W. F. Brown, Thermal Fluctuations of a Single-Domain Particle, *Phys. Rev.* **130**, 1677 (1963).
- [9] Z. Liu, P.-W. Huang, G. Ju, and R. H. Victora, Thermal switching probability distribution of L10 FePt for heat assisted magnetic recording, *Appl. Phys. Lett.* **110**, 182405 (2017).
- [10] A. Venugopal, T. Qu, and R. H. Victora, Non-linear parallel pumped FMR: Three and Four magnon processes, *IEEE Trans. Microw. Theory Tech.* **68**, 602 (2020).